

Article

Numerical Study of the Effect of Flap Geometry in a Multi-Slot Ducted Wind Turbine

Antonio García Auyanet and Patrick G. Verdin * 

School of Water, Energy and Environment, Cranfield University, Cranfield MK43 0AL, UK

* Correspondence: p.verdin@cranfield.ac.uk

Abstract: One possible way to harness wind more efficiently in low-wind urban areas is to place wind turbines inside a duct. A known issue of such approach is due to the flow separation that can occur at the diffuser walls. This can be avoided using a channelled structure consisting of a duct and a flap, also known as a multi-slot system. The present work describes the effects of a flap geometry on the turbine performance, through computational fluid dynamics (CFD). Four flaps based on airfoils, with different thicknesses and cambers, were evaluated. It was found that thinner and more cambered flaps produce higher wind turbine performance, showing power augmentations up to 2.5 compared to a bare turbine. A comparison between the multi-slot design and a single-piece duct of the same geometry was also performed, showing that the multi-slot design is more efficient if the flow is maintained attached to the flap.

Keywords: computational fluid dynamics (CFD); small-scale wind energy; diffuser augmented wind turbines (DAWT); multi-slot diffuser; power coefficient



Citation: García Auyanet, A.; Verdin, P.G. Numerical Study of the Effect of Flap Geometry in a Multi-Slot Ducted Wind Turbine. *Sustainability* **2022**, *14*, 12032. <https://doi.org/10.3390/su141912032>

Academic Editor: Md. Hasanuzzaman

Received: 31 August 2022

Accepted: 22 September 2022

Published: 23 September 2022

Publisher's Note: MDPI stays neutral with regard to jurisdictional claims in published maps and institutional affiliations.



Copyright: © 2022 by the authors. Licensee MDPI, Basel, Switzerland. This article is an open access article distributed under the terms and conditions of the Creative Commons Attribution (CC BY) license (<https://creativecommons.org/licenses/by/4.0/>).

1. Introduction

The use of wind as an alternative source of energy has been in the spotlight in recent years to reduce the consumption of fossil fuels. Large-scale horizontal axis wind turbines have been representing most of the wind power capacity. However, small-scale turbines, typically of diameters ranging from 0.5 to 10 m [1], have gained popularity to increase renewable sources in the electricity mix, at household level. A possible approach to improve the power output of small-scale turbines is to surround these turbines by a duct. When considering such approach, the low pressures induced by the duct at its exit increase the mass of air directed towards the rotor, and thus, the amount of kinetic energy that can be extracted [2]. These devices are known as diffuser augmented wind turbines (DAWT) [3]. Although augmentation technologies have also been studied for vertical axis wind turbines [4], their inherent lower power production has led to more research being focused on horizontal axis ones [3].

One of the first theoretical approaches to DAWT is the work by Lilley and Rainbird in 1956 [5], where the authors reported the duct exit area and the negative pressure coefficients at the diffuser exit as critical parameters for power augmentation. The reduction in tip losses was also highlighted as an important effect. Later, in the 1980s, Foreman et al. [6,7], and Igra [8,9], developed further the concept of ducted turbines. Foreman et al. [6,7] derived theoretical models for DAWT and performed experimental testing of different duct geometries using screens to simulate the turbine rotor. The authors reported a power augmentation factor, i.e., the ratio between the obtained power coefficient and the Betz limit for bare turbines, of nearly 2 [7]. Igra [8,9] carried out a thorough study on DAWT, from a theoretical analysis to an experimental approach in a wind tunnel, leading to a full-scale 3 m diameter pilot turbine. The prototype power augmentation was reported to reach values of about 2.36 [9].

More detailed theoretical models were developed later by Hansen et al. [10] in 2000 and Jamieson [11,12] in 2008 and 2009. Hansen et al. [10] showed that the increase in the

power coefficient for a ducted rotor compared to a bare one is proportional to the ratio of their respective mass flows. They validated the relationship using Computational Fluid Dynamics (CFD) simulations. Jamieson [11,12] went further and generalized the theoretical power extraction of ducted turbines by extending the actuator disc model for bare turbines. The author found out that the theoretical maximum power coefficient for a certain ducted system, or any general system that affects the axial induction, is $16/27(1 - a_0)$, with a_0 being the axial induction factor at the rotor plane without the rotor [11].

The above-mentioned studies, among many others, laid the groundwork for more recent research on DAWT. For example, experiments from Ohya et al. [13,14] and Kanya and Visser [15] provided promising outcomes. Ohya et al. [13,14] developed what they called a “wind-lens”, which consists of a diffuser with a brim, or flange, at its end. For such device, the vortex separation caused by the brim reduces the pressure at the diffuser exit, increasing the mass flow and providing power augmentations up to about 2–5 compared to a bare rotor. Kanya and Visser [15] coupled the rotor design with the flow field induced by the duct to optimise the blades for the non-uniform velocity profile created inside the duct. They reported power coefficients more than 2 times higher than for their open rotor.

A thorough understanding of the flow inside a duct appeared necessary to generate optimal designs. This motivated several numerical studies looking at various DAWT parameters. For example, research was performed on the effects of the diffuser geometry and size [2,16–20] or more specific aspects such as the impact of the tip clearance on the flow behaviour [21].

Among the numerical results and discussions reported in the literature, there is a common agreement regarding the effect of flow separation at the diffuser walls. Flow separation reduces the pressure recovery inside the diffuser. This prevents the pressure behind the turbine to reach values as low as if the flow stayed attached, decreasing the amount of air that passes through the rotor [2]. This phenomenon is depicted in Figure 1. A common practice to reduce this effect is to use airfoil-based ducts, with an aerodynamic shape instead of a conical one [22]. However, separation can still occur on airfoil-based diffusers [16,19]. One possible approach to avoid flow separation is to introduce slots near the diffuser exit. Slots allow external air into the diffuser, providing energy to the boundary layer of the expanding flow and preventing its separation. Such a device is known as a multi-slot diffuser [3,22] and its working principle is illustrated in Figure 1.

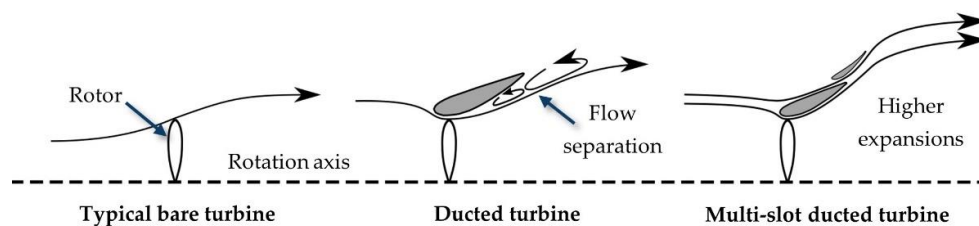


Figure 1. Illustration of the flow behaviour in a bare, ducted and a multi-slot ducted wind turbine.

The concept of injecting external air at the diffuser exit was introduced in the original works on DAWT by Foreman et al. [6,7] and Igra [8,9], in which the beneficial effects of reducing flow separation were reported. Recent studies by Koc and Yavuz [23] and Dighe et al. [24] in 2019 described numerical studies on multi-slot diffusers, created by adding a ring-shaped flap, as originally proposed by Igra [9]. Both studies consisted of a 2D analysis aiming at optimising parameters such as the flap angle and the slot size, among others, approximating the turbine rotor with an actuator disc model. An example of this type of multi-slot diffuser is shown in Figure 1.

Apart from the above-mentioned examples, there have been other interesting ideas on multi-slot diffusers, such as from Sridhar et al. [25] in 2022, with slits at the inlet and holes at the diffuser. However, the ring-shaped flap has been the multi-slot design that has attracted more interest. For example, Siavash et al. [26] in 2020 investigated experimentally ducted turbines with an annular gap at the diffuser.

The purpose of the present study is thus to numerically investigate the multi-slot diffuser concept with a flap added to the main duct, similarly to the one proposed by Igra [9] and numerically researched by Koc and Yavuz [23], and Dighe et al. [24]. The studies described in [23,24] have evaluated parameters such as the flap angle and the slot size, but on a fixed flap geometry. However, the shape of the flap can have an impact on both the flow going through the slot and the expansion behaviour after the flap. Therefore, the present work focuses on the effects of the flap geometry on the turbine performance by testing four flap geometries based on airfoils with different cambers and thicknesses. Additionally, a comparison between the multi-slot diffuser and a single-piece duct is carried out to assess the impact of the flow injection.

Section 2 presents the methodology followed in the research, introducing the turbine and duct specifications, and describing the numerical approach. The main results of the study are then discussed in Section 3. Finally, the relevant conclusions are drawn in Section 4.

2. Materials and Methods

The multi-slot diffuser was analysed using steady 3D CFD simulations on a specific turbine rotor. The rotor was modelled first and validated against experimental data. The duct designs were then created and numerically analysed. The computational grids were generated with the ANSYS Fluent meshing tool and the flow solution obtained with the ANSYS Fluent flow solver.

2.1. Turbine Modelling and Evaluation

The turbine selected was an optimised three-bladed rotor with a diameter of 0.72 m, designed and tested by Hsiao et al. [27], with the blades based on NACA4418 airfoils. The dimensions of the hub geometry were not specified in the original work, so the whole rotor was modelled in the present study as per Figure 2.

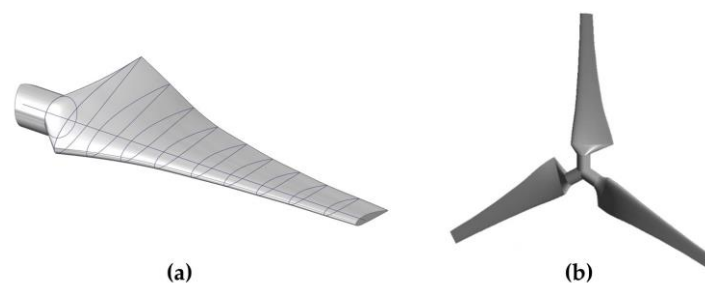


Figure 2. Illustrations of (a) the blade and (b) the whole rotor of the turbine studied.

To evaluate the performance of both the bare and the ducted turbines, two main parameters were investigated. The first one was the power coefficient, C_p . The power was obtained by multiplying the torque produced by the rotor T (N·m) by its rotational speed ω (rad/s), as provided in Equation (1). Hsiao et al. [27] reported a maximum power coefficient $C_p = 0.428$ for the turbine studied, at a wind speed of 10 m/s. The second parameter was the thrust coefficient C_T , presented through Equation (2), which consists of the nondimensionalization of the thrust produced by the wind on the rotor, denoted F (N). The power and thrust coefficients are known to change with the rotational speed of the rotor for a specific wind velocity. This rotational speed is described by the tip speed ratio λ , shown in Equation (3).

$$C_p = \frac{P}{\frac{1}{2}\rho V_0^3 A} = \frac{T\omega}{\frac{1}{2}\rho V_0^3 A} \quad (1)$$

$$C_T = \frac{F}{\frac{1}{2}\rho V_0^2 A} \quad (2)$$

$$\lambda = \frac{\omega R}{V_0} \quad (3)$$

where ρ is the air density (kg/m^3), V_0 is the freestream wind velocity (m/s), R is the rotor radius (m) and A is the reference area (m^2).

There is no general agreement in the literature regarding which area should be considered for the calculation of the power and thrust coefficients of ducted turbines. A common approach is to consider the area of the rotor. However, this is subject to discussion, and it has been argued that it would be more appropriate to use the diffuser exit area to consider the effect of the duct [22]. A clear and universal definition/method should be provided as there are economic considerations involved, when the actual size of the device is incorporated in the definition of the power coefficient [18]. Note that many designs and studies showing power coefficients above the Betz limit of 0.593 using the rotor area definition, would actually produce values below that limit if the duct exit area was used instead in the calculations [22]. Both approaches were considered in the present study, and C_p and C_p^d were used to characterise the power coefficient calculated using the rotor area, and calculated using the diffuser exit area, respectively. A detailed discussion regarding the values of C_p and C_p^d is carried out in Section 3.2.3.

2.2. Domain and Boundary Conditions

The computational domain used for the simulations is shown in Figure 3. Due to the rotational symmetry of the rotor, only one third of the domain was modelled, reducing the computational requirements. The two resulting interfaces at 120° were set as periodic boundaries. The front and back surfaces of the domain were assigned as inlet and outlet, and the external cylindrical face as a symmetry boundary condition. Regarding the solid surfaces, the blade was set as no-slip wall. The same conditions were applied for the duct when running the DAWT simulations. An internal domain containing the blade was also created to simulate its rotation.

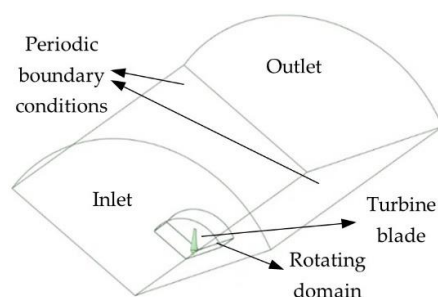


Figure 3. Illustration of the domain employed for the simulations.

The inlet and outlet of the domain were located at a distance of 5 and 10 times the turbine radius, respectively. Another important dimension is the radius of the external cylindrical face as it determines the domain blockage ratio, i.e., the ratio between the turbine swept area and the domain frontal area. Maintaining a similar blockage ratio is important to minimise the impact of the domain boundaries on the flow solution. The radius of the external cylindrical face was thus selected to be 6 times the turbine radius, following considerations from Hsiao et al. [27]. Finally, the top and outlet boundaries were moved back for the ducted cases to a 10 and 20 radius distance, respectively, to maintain a similar blockage ratio and to account for the higher wake produced behind the rotor.

2.3. Duct Geometry Specifications

The geometry of the multi-slot duct tested and the value of its main parameters are presented in Figure 4 and Table 1. A NACA4418 airfoil was used for the duct geometry in the current work. Regarding the rotor location inside the duct, published studies have been carried out to optimise the axial position [18], showing small impact in output power.

It is thus a common practice to place the rotor in the throat of the duct [3,20,28]. With respect to the tip clearance, numerical studies [21] have shown that small clearances can make the tip vortices break more easily, destabilizing the flow near the diffuser wall and producing flow separation. Higher gaps can thus make the tip vortices to re-energize the diffuser boundary layer, delaying flow separation. Based on the results from [21], a high tip clearance of around 3% of the rotor radius was applied to delay flow separation inside the diffuser.

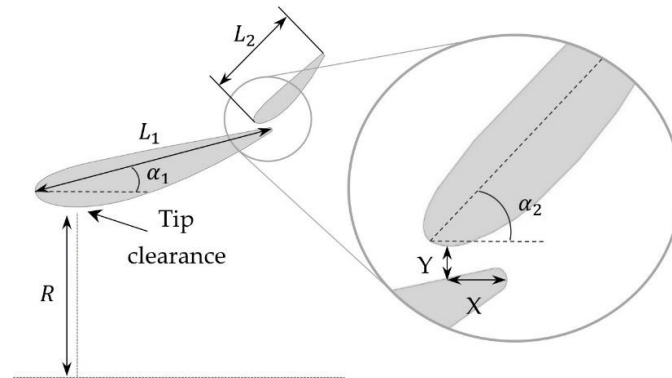


Figure 4. Main parameters of the multi-slot diffuser studied in the present work.

Table 1. Values of the multi-slot diffuser parameters.

Parameter	Value
L_1	75% of $2 \times R = 540$ mm
L_2	40% of $L_1 = 216$ mm
α_1	5° – 30°
X	5% of $L_1 = 27$ mm
Y	~2% of $L_1 = 12$ mm
α_2	15° – 90°

To test the effects of the flap on the turbine performance, four flap geometries were selected: a NACA4418, a Selig S1223, a NACA6409 and a gas turbine blade. A flanged duct was also tested. The flanged case was created using the geometry of the multi-slot duct with the Selig S1223 flap and closing the gap. The four flap geometries considered here and the flanged case are shown in Figure 5.



Figure 5. Two-dimensional schematic of the flap geometries studied in the present work.

The NACA4418, Selig S1223 and NACA6409 airfoils were selected to test the effect of the flap thickness and camber. The thickness decreased from the high value of the NACA4418 airfoil to an almost flat case, resembling a conical flap, with the NACA6409 airfoil. The Selig shows an intermediate thickness while having a high camber compared to the two previous airfoils. The final geometry was based on an airfoil with extremely high camber, similarly to the ones used in gas turbine blades. This was considered to evaluate whether a large nozzle region at the leading edge of the flap improves the flow reenergization inside the slot. The geometry of this flap was extracted from [29].

The length of the flap considered in [24] was equal to 35% of the duct length and was kept constant. This was optimised in [23], resulting in an optimal value at 40% of the duct

length. A length of flap corresponding to 40% of the duct length was therefore considered here. Other important parameters included the horizontal and vertical position of the flap lowest point, denoted X and Y, respectively, and the flap angle, α_2 . The horizontal and vertical dimensions for the slot were also based on parametric optimisations carried out in [23,24].

2.4. Numerical Models

2.4.1. Governing Equations

The evaluation of the different turbine designs was carried out through steady 3D Reynolds-Averaged Navier–Stokes (RANS) CFD simulations with the commercial software ANSYS Fluent. The SIMPLE scheme was selected for the pressure-velocity coupling and a second order spatial discretisation was used for an improved accuracy. The RANS continuity and momentum equations can be written as [30]:

$$\frac{\partial \bar{u}_i}{\partial x_i} = 0 \quad (4)$$

$$\rho \frac{\partial \bar{u}_i}{\partial t} + \rho \bar{u}_j \frac{\partial \bar{u}_i}{\partial x_j} = -\frac{\partial \bar{P}}{\partial x_i} + \frac{\partial}{\partial x_j} \left(\mu \frac{\partial \bar{u}_i}{\partial x_j} \right) - \frac{\partial \overline{\rho u'_i u'_j}}{\partial x_j} \quad (5)$$

where \bar{P} and \bar{u} are the time-averaged pressure and velocity, and μ is the air dynamic viscosity. The value $-\overline{\rho u'_i u'_j}$ corresponds to the Reynolds stress tensor, a quantity dependent on the fluctuating component of the velocity, denoted \bar{u}' [30].

Two turbulence models are commonly used for simulating ducted turbines, the $k - \omega$ SST and the $k - \varepsilon$ models. The $k - \omega$ SST model has been proven to provide accurate predictions of flows where separation is present [31]. This model switches automatically from a $k - \omega$ formulation near the walls to the $k - \varepsilon$ definition in the bulk flow [32] and has been used in several numerical studies on ducted wind turbines [10,16,17,19,24,25]. Some other works considered some variant of the $k - \varepsilon$ model, which also provided reasonable predictions of the flow behaviour inside ducts [18,20,33]. One of its sub models is the Realizable $k - \varepsilon$, which offers better performance in separated flows compared to the standard $k - \varepsilon$ model [34]. The comparison of both the $k - \omega$ SST and the Realizable $k - \varepsilon$ models against available experimental data is discussed in Section 2.4.3.

Finally, the multiple reference frame (MRF) model was used to simulate the turbine rotation. In the MRF approach, there is a separation in the domain between the rotor and the external regions. The flow inside the rotor region is solved using the RANS equations based on a moving reference frame, allowing to perform steady simulations. This approach reduces the computational requirements and has been proven to provide accurate results when compared to transient simulations [2] and to experimental data [27].

2.4.2. Mesh Generation

Fluent Meshing was used to create the 3D meshes for both bare and ducted turbines. Both $k - \omega$ SST and Realizable $k - \varepsilon$, with the enhanced wall treatment option, require a $y^+ \leq 1$ in the near-wall region to accurately resolve the boundary layer. This was considered in the meshing process, with the addition of inflation layers at the blade and duct walls. A mesh independence study was conducted for each configuration, i.e., bare, ducted, and multi-slot turbines, and the resulting meshes comprised between 2 and 7×10^6 cells. Examples of the meshes generated in this work are provided in Figure 6.

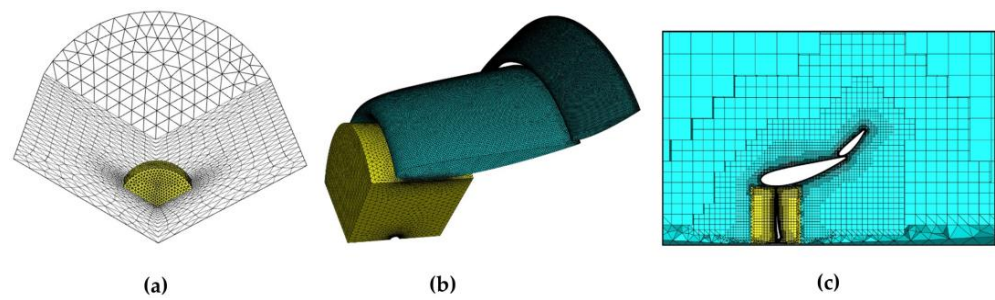


Figure 6. Examples of surface meshes for (a) the bare turbine, (b) the multi-slot case, and (c) volumetric mesh in a section perpendicular to the turbine plane for the multi-slot case.

2.4.3. Numerical Validation and Selection of Design Point

To validate the numerical approach, the bare turbine model was simulated and the results were compared to the experimental data from Hsiao et al. [27]. The first step was to conduct a mesh independence study to find an optimal grid size. This was achieved through evaluating two parameters, the torque and the skin friction coefficient produced by the wind on the blade, at one operational point. The conditions for this study were a wind speed of 10 m/s, similarly to the one tested experimentally in [27], and with a tip speed ratio of 5, which is the point of maximum efficiency reported in [27]. The results are shown in Figure 7. A mesh of around 4×10^6 cells provided results with less than 1% difference compared to the finest mesh tested, this mesh was thus selected for the study.

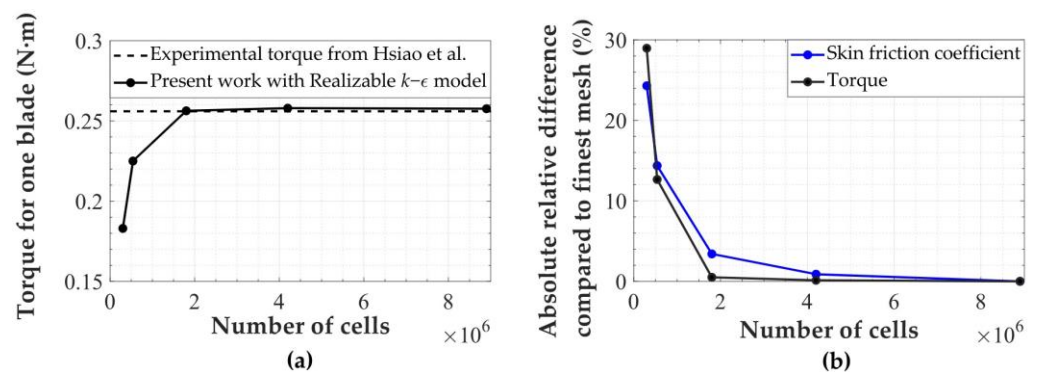


Figure 7. Result of the mesh independence study for the bare turbine conducted with the Realizable $k - \epsilon$ model: (a) Torque obtained and comparison against the experimental value by [27], (b) relative difference of the torque and skin friction coefficient compared to the finest mesh tested.

With a suitable mesh selected, the turbine was simulated at other $TSRs$ and the resulting power coefficient was compared with the data obtained both experimentally and numerically by Hsiao et al. [27]. Such comparison is shown in Figure 8. The obtained C_p values using the Realizable $k - \epsilon$ turbulence model provided a better agreement with the results from Hsiao et al. [27] compared to those obtained with the $k - \omega$ SST model. The Realizable $k - \epsilon$ model predicted C_p values with less than 10% difference compared to the experimental data in the range of λ tested. CFD simulations based on this model also accurately reproduced the shape of the experimental curve. However, the $k - \omega$ SST model underpredicted the C_p at low λ , and overpredicted it at high λ .

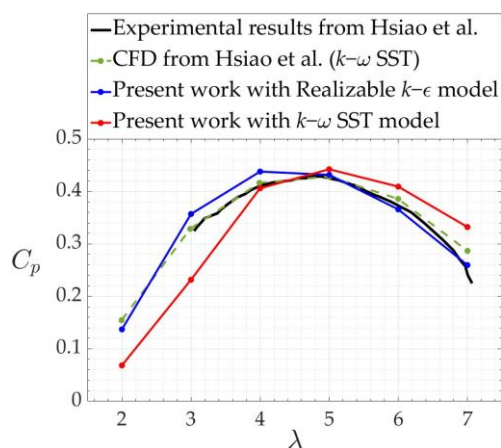


Figure 8. Comparison of the C_p values obtained numerically in the present study with the experimental and numerical results from Hsiao et al. [27].

To understand the discrepancy between the results obtained with both turbulence models, a 2D study of the lift and drag on a NACA4418 airfoil was performed, this airfoil being used for the blades of the turbine investigated in this work. The domain considered for the airfoil study is shown in Figure 9. The airfoil chord length was 1 m and the inlet velocity was 1.45 m/s, to have a Reynolds number at the blades of 10^5 . Regarding the domain size, the inlet and outlet were located at a distance of 20 and 40 times the airfoil chord length, respectively. A structured mesh was created using the mesh generator ICEM CFD. The spacing of the cells near the airfoil was set to obtain a y^+ value less than 1, as required by the turbulence models considered. A mesh of around 170,000 cells was selected after conducting a mesh independence study.

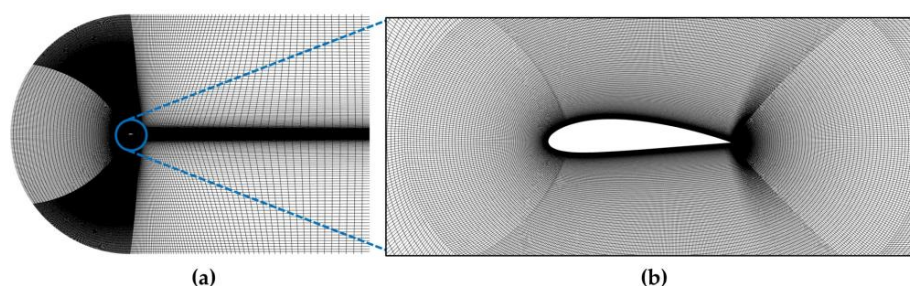


Figure 9. (a) Domain considered to study the lift and drag coefficients of the NACA4418 airfoil and (b) detail of the mesh around the airfoil.

The obtained lift and drag coefficients, C_L and C_D , respectively, are shown in Figure 10. The Realizable $k-\epsilon$ model predicted the lift behaviour with accuracy for a wide range of angles of attack, including the stall region, compared to experimental data from [35]. However, the $k-\omega$ SST model highly underestimated the lift coefficient and underpredicted the stall angle. Additionally, even though neither model showed a close agreement on drag coefficient, the Realizable $k-\epsilon$ model provided a similar trend to the experimental data.

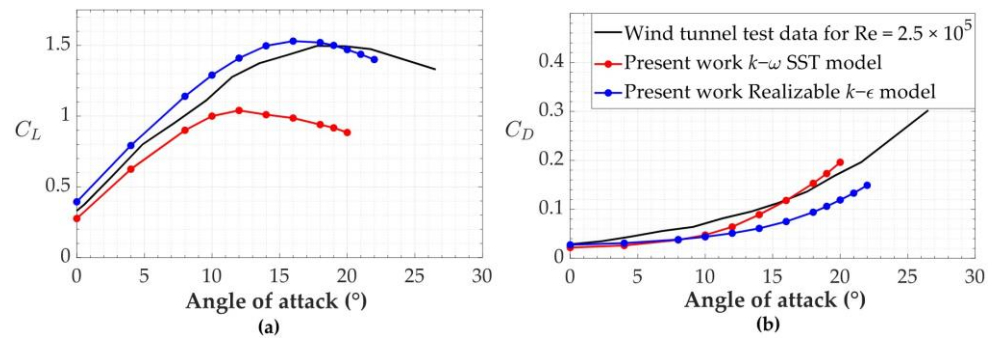


Figure 10. (a) Lift and (b) drag coefficients on a NACA 4418 airfoil obtained in the present work with Fluent using two different turbulence models at $Re = 10^5$, and comparison against experimental data for $Re = 2.5 \times 10^5$ from [35].

Results in Figure 10 explain the difference between the two turbulence models seen in Figure 8. At low λ , the angle of attack on the blade is high, between 10° and 15° [27], and in those conditions the $k - \omega$ SST model provides low lift and high drag values, this explains the underprediction of the C_p values in Figure 8. However, at high λ , the drag starts to become predominant due to the low angles of attack. In those conditions the $k - \omega$ SST model provides lower drag values, resulting in higher C_p predictions. Based on the above results and analysis, the Realizable $k - \epsilon$ model was selected for the rest of the simulations on the turbine.

The turbine model being validated, a design point was selected for the study of the ducted cases. Hsiao et al. [27] performed experimental testing of the turbine at a wind speed $V_0 = 10$ m/s, which is unrealistic for an urban environment. Therefore, a wind speed $V_0 = 5$ m/s, and a tip speed ratio of $\lambda = 5$ were considered as design point.

3. Results and Discussion

This section presents the main outcomes of the research. Firstly, the effect of surrounding the rotor by a simple duct is discussed, and the obtained power augmentations are compared with the theoretical predictions for ducted turbines. Then, the results of the evaluation of the multi-slot flap geometry are summarised.

3.1. Simple Ducted Turbine

The main principle of DAWTs is based on the mass flow increment inside the duct. A theoretical analysis developed by Hansen et al. [10] showed a proportional relationship between the power enhancement of the turbine and the ratio of mass flows, denoted \dot{m} , for the ducted and bare rotors. This relation is presented in Equation (6).

$$\frac{C_{pd}}{C_{pb}} = \frac{C_{Td}}{C_{Tb}} \times \frac{\dot{m}_d}{\dot{m}_b} \quad (6)$$

where Subscript d and b refer to the ducted and bare turbines, respectively. The term C_{Td}/C_{Tb} in Equation (6) was not presented by Hansen et al. [10] as their theoretical analysis was established through comparing the same C_T for the ducted and bare cases. As a specific rotor was used in the present work, the value of C_{Td} and C_{Tb} were imposed by the rotor and had different values. Therefore, this term had to be included in Equation (6).

The duct geometry presented in Section 2.3 was simulated without the flap. A mesh independence study was conducted first, looking at the blade torque and the thrust on the duct. The corresponding results are shown in Table 2. A grid comprising around 2.5×10^6 cells is seen to provide mesh independent results and increasing the number of cells will not produce much difference in the results; this mesh was therefore selected. Simulations were then carried out for the ducted turbine at different duct angles. The main results in terms of the rotor power and thrust coefficients, and mass flow rates are shown in Figure 11.

Table 2. Results of the mesh independence study for the ducted turbine with NACA4418 duct at an angle of 10° . Study conducted at $V_0 = 5$ m/s and $\lambda = 5$. The relative difference compared to the finest mesh tested is provided in brackets (%).

Mesh	Number of Cells	Torque on One Blade (N·m)		Thrust on Duct (N)	
1	2.5 M	0.07204	(+0.54%)	0.646	(+1.095%)
2	5 M	0.07175	(+0.14%)	0.6458	(+1.064%)
3	8.6 M	0.07165		0.639	

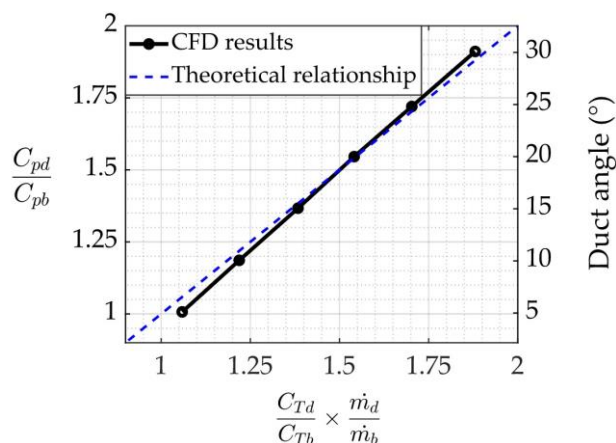


Figure 11. Comparison between CFD-based results obtained for the ducted turbine and the theoretical relationship in Equation (6).

Figure 11 shows an almost linear power enhancement as the duct angle is increased. This comes along with the same trend as for the thrust coefficient. Those results are in line with the theoretical relationship presented in Equation (6). It is worth noting that a slight deviation is present in the CFD-based results. This can be attributed to viscous effects and/or flow conditions such as the air going through the tip clearance and/or the non-uniform velocity at the rotor, which are not considered in the assumptions of the 1D theoretical analysis. Note also that CFD results from Hansen et al. [10] showed a similar difference with the theoretical values [36].

For a deeper insight into the duct flow, the velocity contours are plotted in the middle section of the duct in the axial direction, for several duct angles, see Figure 12. The area of expansion increases with the diffuser outlet area, producing higher velocities at the rotor plane, and lower ones in the wake outside the duct.

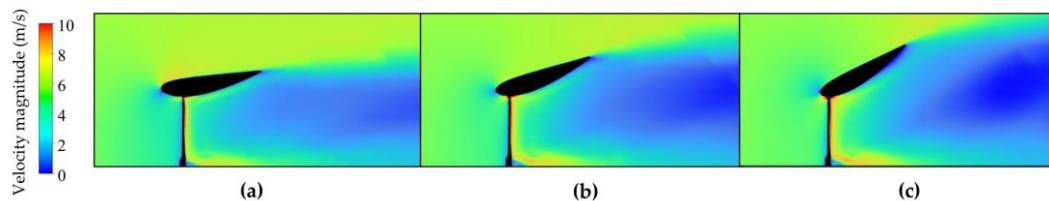


Figure 12. Contours of velocity magnitude in a plane perpendicular to the rotor for different duct angles: (a) 10° , (b) 20° and (c) 30° , at $V_0 = 5$ m/s and $\lambda = 5$.

One important aspect to highlight is that flow separation on the diffuser walls was not detected for any of the angles simulated, as seen in Figure 12. This occurs despite the angle of attack for the duct being higher than the stall angle for the airfoil constituting the duct. The reason is that the pressure drop induced by the rotor makes the flow prone to important expansions to increase its pressure, maintaining it attached to the walls for higher diffuser angles. This has been reported in previous studies [28] and the effects are more important for high thrust coefficients, as in the case of the turbine studied here.

To conclude the duct analysis, a duct angle was selected to serve as a base for the multi-slot case. An angle of 15° was thus chosen to achieve a compromise between power enhancement and diffuser exit area, as high exit areas can affect the C_p^d values. This is further discussed in Section 3.2.3. Examples of the streamlines for the selected duct and a comparison with the bare turbine are shown in Figure 13. It can be seen that the expansion behind the rotor is more significant for the ducted turbine than for the bare one. Additionally, the mass flow increase can be seen through a larger stream section that is directed towards the rotor.

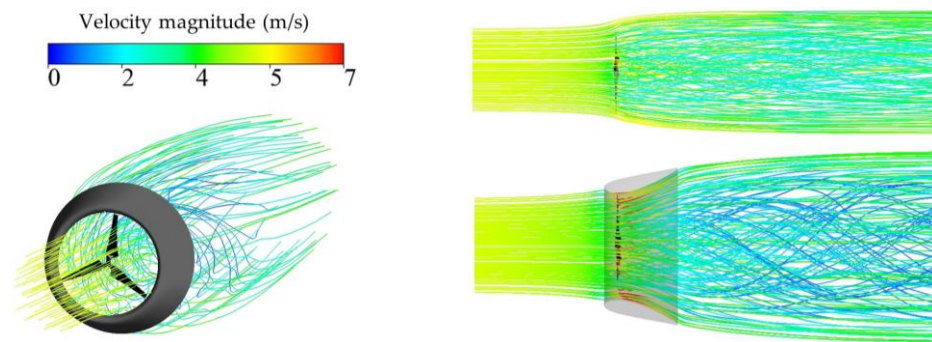


Figure 13. Three-dimensional streamlines around the bare turbine (top right) and the ducted turbine with a 15° angle duct (bottom) for $V_0 = 5$ m/s and $\lambda = 5$.

3.2. Multi-Slot Ducted Wind Turbine

The effect of adding a flap to the ducted turbine is discussed in this section. This covers the main objectives of this work, i.e., the 3D numerical simulation of different multi-slot flap geometries and the comparison with a flanged duct. The study of the flap geometry is presented first. Then, the effects due to the removal of the slot are assessed in detail. Finally, a discussion is carried out on the appropriateness of the multi-slot design.

3.2.1. Effect of the Flap Geometry on the Turbine Performance

The multi-slot flap geometries to be tested were introduced in Section 2.3. Before the evaluation of the different cases, a mesh independence study was conducted for the multi-slot duct with a NACA4418 flap at 45° . The two parameters evaluated were the torque on the turbine blades and the thrust produced on the flap. The results are summarised in Table 3. A mesh comprising around 6.6×10^6 cells provided mesh independent values.

Table 3. Result of the mesh independence study for the multi-slot ducted turbine with a NACA4418 flap at 45° . Study conducted at $V_0 = 5$ m/s and $\lambda = 5$. The relative difference compared to the finest mesh tested is provided in brackets (%).

Mesh	Number of Cells	Torque on One Blade (N·m)		Thrust on Flap (N)	
1	3.8 M	0.1271	(+2.5%)	2.993	(+1.42%)
2	6.6 M	0.1239	(−0.08%)	2.955	(+0.14%)
3	8.1 M	0.124		2.951	

The evaluation of the four flap geometries was performed by simulating each case at the angles described in Section 2.3. The results in terms of power coefficient considering both the rotor and duct exit area are shown in Figure 14. It is worth mentioning that the nozzle part for the case of the gas turbine blade flap disrupted the flow at low angles due to its high camber, so only the results for angles above 30° are presented for that geometry.

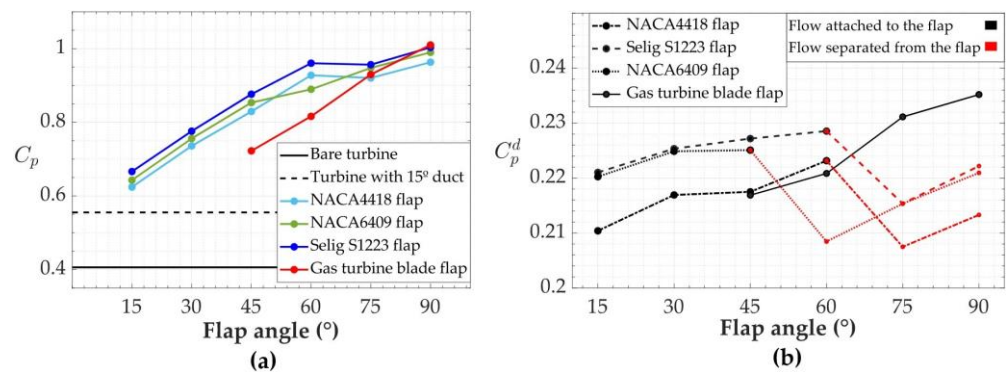


Figure 14. Results for the different flap geometries studied in terms of (a) power coefficient, (b) power coefficient considering the duct exit area. Results for $V_0 = 5$ m/s and $\lambda = 5$.

Figure 14a shows a power increase trend with the flap angle until a certain value from which the trend decreases. The decrease does not happen for the gas turbine blade due to the effects mentioned in the previous paragraph. The change in trend is due to the flow separation taking place on the flap wall, depicted in red colour in Figure 14b.

Based on the previous results, conclusions can be drawn. Regarding the NACA and Selig airfoils, thinner and more cambered geometries provided higher power outputs, both before and after flow separation. The lower power outputs for the thicker flap geometry could be attributed to the presence of higher viscous losses. On the other hand, more cambered geometries increase the circulation induced by the flap, producing higher flow expansions at the duct exit and, thus, larger power outputs. Additionally, the use of an almost conical flap such as the one based on a NACA6409 airfoil, caused flow separation at lower angles compared to the other airfoils. Note that the highest power outputs for the NACA and Selig airfoils were obtained for flaps at 90° , where important flow separation takes place. However, the power coefficient considering the duct exit area in those conditions is lower compared to the cases with attached flow.

The best results for both power coefficients considered were achieved for the gas turbine blade at 90° , with an increase in total power of almost 2.5 times compared to the bare turbine. The camber of that airfoil maintained the flow attached even for such high angles. Therefore, the most efficient designs for the multi-slot were found for the highest flap angles at which the flow stayed attached. Details of the flow behaviour inside the duct for different flap angles are shown in Figure 15 for the Selig case.

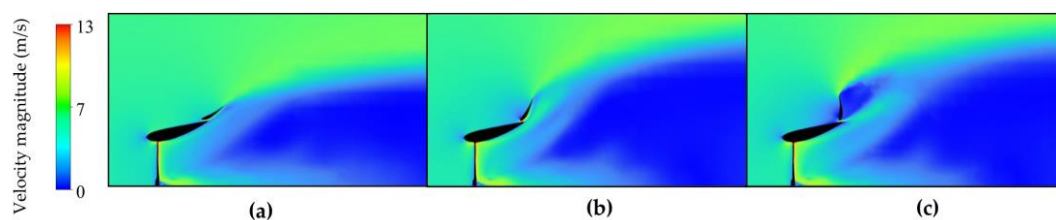


Figure 15. Contours of velocity magnitude in a plane perpendicular to the rotor for the Selig flap at different angles: (a) 30° , (b) 60° and (c) 90° at $V_0 = 5$ m/s and $\lambda = 5$.

In line with the conclusions drawn for the simple duct in Section 3.1, Figure 15 shows how the expansion of the flow is enhanced as the flap angle increases, leading to important flow separation from the flap at high angles. A significant velocity reduction can also be noticed in the wake, caused by the flow expansion, leading to flow recirculation. This is illustrated in Figure 16, showing the streamlines for the multi-slot with the gas turbine blade flap at 90° . The expansion forced by the duct is so important that the wake becomes unstable, causing a prominent recirculation region. The wake for this case corresponds to the turbulent state observed empirically for turbines with high thrust coefficients [37]. This is the main reason for the flow to remain attached, even at such high flap angles.

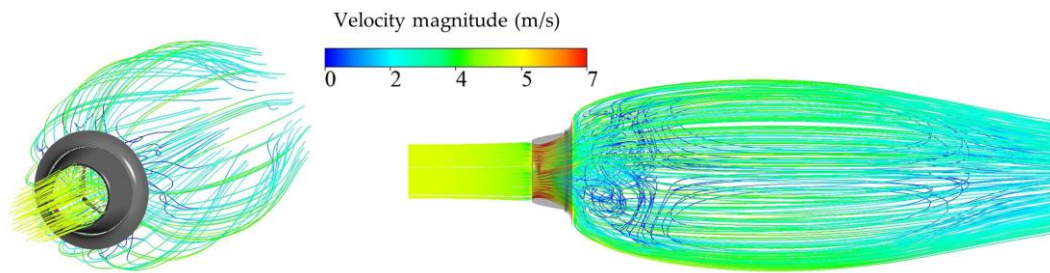


Figure 16. Three-dimensional streamlines around the turbine with a multi-slot duct with a gas turbine blade flap at a 90° for $V_0 = 5$ m/s and $\lambda = 5$.

To conclude the analysis of the multi-slot, a comparison against the bare rotor was carried out for other *TSRs*. The corresponding results are shown in Figure 17, where the $C_p - \lambda$ curve is presented. As can be seen, a maximum value $C_p = 1$ was achieved at $\lambda = 5$ for the multi-slot design with the best performance, i.e., with the gas turbine blade flap at 90° . Two main differences can be highlighted between the curves for the bare and ducted turbines. The first one is that the optimal operational region became narrower for the ducted case, and the other one is that the maximum efficiency point shifted to a slightly higher λ . Both effects were studied in a systematic review of DAWTs in [22], where 34 ducted turbines from the literature were analysed, showing that around 76% of them presented a narrower operational range, and 56% provided a higher optimal λ . Although the first effect is not desirable as it requires more control to maintain the turbine in its optimal region, the second one allows the turbine to work at lower wind speeds [22].

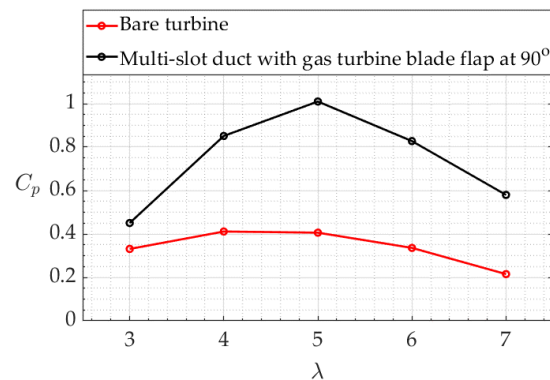


Figure 17. $C_p - \lambda$ curves of the bare and multi-slot ducted turbines for $V_0 = 5$ m/s.

3.2.2. Comparison of the Multi-Slot with a Flanged Duct

Multi-slot diffuser simulation results are now compared to simulation results obtained with a flanged duct, see Figure 18. As stated in Section 2.3, the flanged duct was constructed by closing the slot between the duct and the flap, thus making a single-piece diffuser.

As can be seen in Figure 18, both cases provide very similar results for low angles, when the flow is attached. However, as the angle increases and the flow starts separating, the flanged duct progressively shows lower performance. The flow separation was gradual for the flanged duct whereas it was rather abrupt for the multi-slot case. Once the flow is completely separated in both cases, the flanged duct provided slightly higher power outputs compared to the multi-slot.

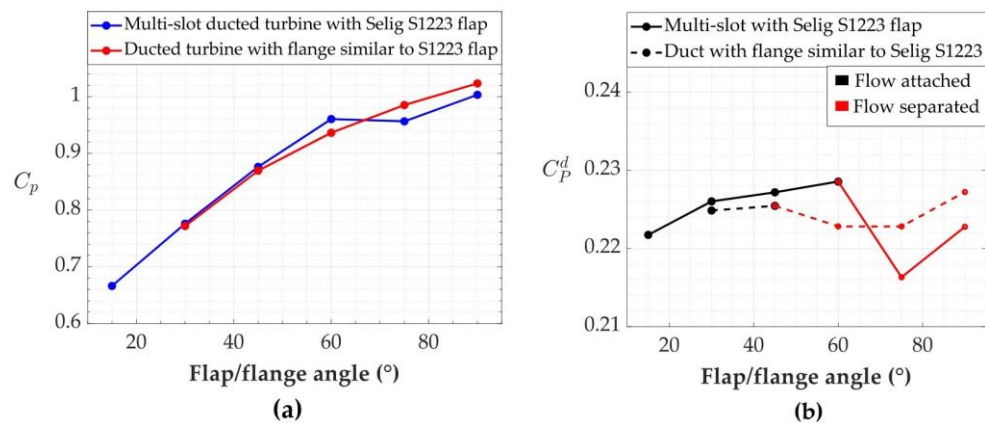


Figure 18. Comparison of the results between the multi-slot and the flanged ducts in terms of power coefficient considering (a) the rotor area and (b) the diffuser exit area at $V_0 = 5$ m/s and $\lambda = 5$.

Two clear trends can be seen from Figure 18 in terms of comparative performance. If the flow can be maintained attached to the flap, the multi-slot provides higher performance than the flanged duct. This difference is broadened as the flow progressively separates from the flap. After a critical point at which the flow also separates from the flap, the multi-slot shows a reduction in efficiency compared to the flanged diffuser. A possible explanation for the lowering of the efficiency of the multi-slot after flow separation is provided in Figure 19, showing the velocity contours for the two cases with a 90° flap/flange.

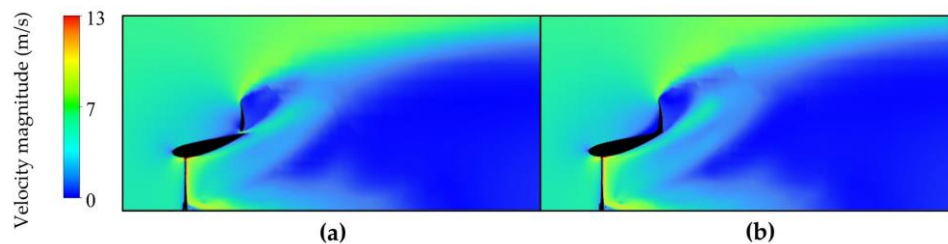


Figure 19. Velocity contours for (a) the multi-slot and (b) the flanged ducts with a Selig S1223 flap/flange at 90° at $V_0 = 5$ m/s and $\lambda = 5$.

As illustrated in Figure 19, the injection of external air when the flow is separated from the flap does not allow as high expansions as for the flanged case. This can be explained by the fact that the injection makes the separation vortex smaller, reducing the effective exit area. Another effect is that the injected air also needs to expand once it passes the slot, allowing lower expansions for the flow passing through the rotor.

Therefore, although the highest power produced for the multi-slot was obtained when the flow is separated from the flap for the Selig and NACA airfoils at 90° , a flanged duct is a better option in those conditions. It is worth noting that the reference work by Koc and Yavuz [23] also obtained the maximum velocity augmentation on the rotor with a high flap angle that caused flow separation from the flap. However, the authors in [23] did not compare the result with a flanged duct of the same geometry.

3.2.3. Appropriateness of the Multi-Slot Design on the Rotor Studied

To conclude, a brief discussion is carried out regarding the augmentation effect of the multi-slot compared to other DAWTs from the literature. A systematic review of DAWT carried out by [22] showed that 85% of the 60 turbines they extracted from the literature presented a C_p higher than the Betz limit, with an average value of 0.75. Although a maximum C_p value of 1 was obtained in the present research, the figure falls to a $C_p^d = 0.235$ when the exit area of the diffuser is used as reference. The analysis from [22] showed that the average C_p^d for the 60 turbines studied was 0.37, situating the DAWT of the present

study below the average of the literature reviewed by [22]. This outcome is due to two main reasons. Firstly, as the purpose of the current work was to study the multi-slot, high diffuser exit areas were used to analyse the flow separation effect and to account for the flap size. Indeed, the area ratio between the diffuser exit and the rotor presented values between 3 and 4.5 in the present study. Similar numerical works on multi-slot diffusers [23,24] also considered cases with area ratios of that order. However, the review from [22] showed that large area ratios lead to low values of C_p^d , flow separation being one explanation for such effect. Another cause is that the relative increase in power output for large area ratios is smaller compared to the increase in exit area. This can be seen in Figure 14, where C_p^d values are lower than the C_p of the bare turbine, even when separation is not present. Note that all 10 cases analysed by [22] with area ratios higher than 2.5 presented C_p^d values below the mean.

The second reason for obtaining this low C_p^d is that the turbine rotor selected here already had a high bare performance, with a C_p of 0.41 at the design point. The review from [22] showed that it is more difficult to achieve high C_p^d values for ducted turbines with high performance bare rotors. For instance, none of the 13 cases analysed by [22] with C_p values higher than 0.4 for the bare rotor provided an improvement in C_p^d .

Based on the previous considerations, the multi-slot might not be the best option for a turbine with high power and thrust coefficients, like the case studied here. To obtain higher C_p^d values, the diffuser exit would need to be reduced. Although this could be achieved with the multi-slot diffuser by reducing the flap length, a flanged duct might be a better option for such case. The flanged duct could allow similar expansions to the multi-slot, as the results showed in Section 3.2.2, but with a smaller and more compact diffuser. This is illustrated in Figure 20.

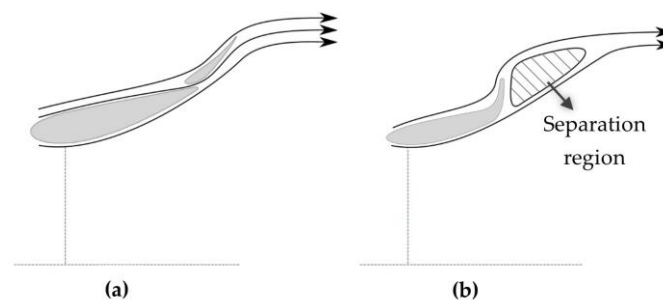


Figure 20. Illustration of the comparison of flow behaviour between (a) a multi-slot and (b) a compact flanged duct.

Figure 20 shows that the separation region on a flanged duct acts like a wall guiding the air, leading to high flow expansions. This is the principle behind the “wind-lens” described by Ohya et al. [13,14], and discussed in Section 1, which provided high C_p^d values even for a high C_p bare rotor. Note that the separation region angle is conditioned by the diffuser angle. Thus, this design could be a good option for high thrust turbines like the one studied here, as the diffuser can have a high angle without leading to flow separation before the flange. Therefore, for a turbine rotor with high values of thrust coefficient and bare performance, a compact flanged duct seems a better option, in terms of efficiency, than the multi-slot diffuser.

An interesting aspect would be to carry out the same study on a bare rotor in the future, with lower power and thrust coefficients. In that regard, the theoretical study on DAWT by Jamieson [11] showed that the optimum rotor performance for ducted devices is achieved for a thrust coefficient $C_T = 8/9$, the same as for bare turbines. In contrast, the rotor studied here presented a $C_T = 0.96$, with even higher values for the ducted cases, reaching up to $C_T = 1.46$ for the multi-slot case.

The maximum differences in performance between the multi-slot and flanged ducts in Section 3.2.2 were around 2–3%. These low differences may be caused by the important

expansion induced by the rotor with a high thrust coefficient, which maintained the flow attached for large diffuser angles. The difference could be expected to be higher for rotors with lower thrust coefficients. Therefore, an optimal approach would be to select a bare rotor providing a C_T around the optimal value of 8/9 when ducted.

4. Conclusions

The design and the analysis of a ducted wind turbine with a multi-slot diffuser were performed. The main objective was to carry out 3D numerical simulations of the multi-slot duct and evaluate the effect of the flap geometry. It was found that thinner and more cambered flaps provide higher power enhancements. In that sense, the best results were achieved with a flap geometry based on a gas turbine blade at 90°, providing a power coefficient almost 2.5 times higher than for the bare turbine.

The second objective was to compare the multi-slot diffuser with a flanged one, created by eliminating the slot. Two trends were highlighted in that comparison. Firstly, the multi-slot provided higher power outputs than the flanged duct until separation from the flap occurred. For higher flap angles, the flanged diffuser improved the performance of the multi-slot. However, as the bare rotor presented a high thrust coefficient, there was a low tendency in flow separation at the diffuser, thus making the difference between the multi-slot and the flanged ducts not remarkable.

As part of future work and recommendations, a similar study as the one conducted here would be of interest, for a turbine rotor with lower power and thrust coefficients. Furthermore, a coupled design of the rotor and duct considering their interaction would be an ideal approach, so that the optimal thrust coefficient value of 8/9 is achieved. This would allow to evaluate if the difference between the multi-slot and flanged diffusers is broadened when a higher flow separation is present inside the duct.

Author Contributions: Conceptualization, A.G.A.; methodology, A.G.A.; investigation, A.G.A.; writing—original draft preparation, A.G.A.; writing—review and editing, A.G.A. and P.G.V.; supervision, P.G.V. All authors have read and agreed to the published version of the manuscript.

Funding: This research received no external funding.

Institutional Review Board Statement: Not applicable.

Informed Consent Statement: Not applicable.

Data Availability Statement: Not applicable.

Conflicts of Interest: The authors declare no conflict of interest.

References

1. Tummala, A.; Velamati, R.K.; Sinha, D.K.; Indrajaya, V.; Krishna, V.H. A review on small scale wind turbines. *Renew. Sustain. Energy Rev.* **2016**, *56*, 1351–1371. [[CrossRef](#)]
2. Jafari, S.; Kosasih, B. Flow analysis of shrouded small wind turbine with a simple frustum diffuser with computational fluid dynamics simulations. *J. Wind Eng. Ind. Aerodyn.* **2014**, *125*, 102–110. [[CrossRef](#)]
3. Agha, A.; Chaudhry, H.N.; Wang, F. Diffuser Augmented Wind Turbine (DAWT) Technologies: A Review. *Int. J. Renew. Energy Res.* **2018**, *8*, 1369–1385. [[CrossRef](#)]
4. Wong, K.H.; Chong, W.T.; Sukiman, N.L.; Poh, S.C.; Shiah, Y.-C.; Wang, C.-T. Performance enhancements on vertical axis wind turbines using flow augmentation systems: A review. *Renew. Sustain. Energy Rev.* **2017**, *73*, 904–921. [[CrossRef](#)]
5. Lilley, G.M.; Rainbird, W.J. *A Preliminary Report on the Design and Performance of Ducted Windmills*; College of Aeronautics: Cranfield, UK, 1956.
6. Oman, R.; Foreman, K.; Gilbert, B. *Investigation of Diffuser-Augmented Wind Turbines. Part II. Technical Report*; Grumman Aerospace Corporation: Bethpage, NY, USA, 1977. [[CrossRef](#)]
7. Foreman, K.; Gilbert, B.; Oman, R. Diffuser augmentation of wind turbines. *Sol. Energy* **1978**, *20*, 305–311. [[CrossRef](#)]
8. Igra, O. The shrouded aerogenerator. *Energy* **1977**, *2*, 429–439. [[CrossRef](#)]
9. Igra, O. Research and development for shrouded wind turbines. *Energy Convers. Manag.* **1981**, *21*, 13–48. [[CrossRef](#)]
10. Hansen, M.O.L.; Sørensen, N.N.; Flay, R.G.J. Effect of Placing a Diffuser around a Wind Turbine. *Wind Energy* **2000**, *3*, 207–213. [[CrossRef](#)]

11. Jamieson, P. Generalized limits for energy extraction in a linear constant velocity flow field. *Wind Energy* **2008**, *11*, 445–457. [[CrossRef](#)]
12. Jamieson, P.M. Beating Betz: Energy Extraction Limits in a Constrained Flow Field. *J. Sol. Energy Eng.* **2009**, *131*, 031008. [[CrossRef](#)]
13. Ohya, Y.; Karasudani, T.; Sakurai, A.; Abe, K.-I.; Inoue, M. Development of a shrouded wind turbine with a flanged diffuser. *J. Wind Eng. Ind. Aerodyn.* **2008**, *96*, 524–539. [[CrossRef](#)]
14. Ohya, Y.; Karasudani, T. A Shrouded Wind Turbine Generating High Output Power with Wind-lens Technology. *Energies* **2010**, *3*, 634–649. [[CrossRef](#)]
15. Kanya, B.; Visser, K.D. Experimental validation of a ducted wind turbine design strategy. *Wind Energy Sci.* **2018**, *3*, 919–928. [[CrossRef](#)]
16. Dighe, V.V.; de Oliveira, G.; Avallone, F.; van Bussel, G. On the Effects of the Shape of the Duct for Ducted Wind Turbines. In *2018 Wind Energy Symposium*; American Institute of Aeronautics and Astronautics: Reston, VA, USA, 2018. [[CrossRef](#)]
17. Dighe, V.; Avallone, F.; Tang, J.; van Bussel, G. Effects of Gurney Flaps on the Performance of Diffuser Augmented Wind Turbine. In *35th Wind Energy Symposium*; American Institute of Aeronautics and Astronautics: Reston, VA, USA, 2017. [[CrossRef](#)]
18. Venters, R.; Helenbrook, B.T.; Visser, K.D. Ducted Wind Turbine Optimization. *J. Sol. Energy Eng.* **2017**, *140*, 011005. [[CrossRef](#)]
19. Shives, M.; Crawford, C. Developing an empirical model for ducted tidal turbine performance using numerical simulation results. *Proc. Inst. Mech. Eng. Part A J. Power Energy* **2011**, *226*, 112–125. [[CrossRef](#)]
20. Khamlaj, T.A.; Rumpfkeil, M.P. Analysis and optimization of ducted wind turbines. *Energy* **2018**, *162*, 1234–1252. [[CrossRef](#)]
21. Avallone, F.; Ragni, D.; Casalino, D. On the effect of the tip-clearance ratio on the aeroacoustics of a diffuser-augmented wind turbine. *Renew. Energy* **2020**, *152*, 1317–1327. [[CrossRef](#)]
22. Nunes, M.M.; Junior, A.C.P.B.; Oliveira, T.F. Systematic review of diffuser-augmented horizontal-axis turbines. *Renew. Sustain. Energy Rev.* **2020**, *133*, 110075. [[CrossRef](#)]
23. Koc, E.; Yavuz, T. Effect of Flap on the Wind Turbine-Concentrator Combination. *Int. J. Renew. Energy Res.* **2019**, *9*, 551–560. [[CrossRef](#)]
24. Dighe, V.V.; Avallone, F.; Igra, O.; van Bussel, G. Multi-element ducts for ducted wind turbines: A numerical study. *Wind Energy Sci.* **2019**, *4*, 439–449. [[CrossRef](#)]
25. Sridhar, S.; Zuber, M.; Shenoy, S.; Kumar, A.; Ng, E.Y.; Radhakrishnan, J. Aerodynamic comparison of slotted and non-slotted diffuser casings for Diffuser Augmented Wind Turbines (DAWT). *Renew. Sustain. Energy Rev.* **2022**, *161*, 112316. [[CrossRef](#)]
26. Siavash, N.K.; Najafi, G.; Hashjin, T.T.; Ghobadian, B.; Mahmoodi, E. An innovative variable shroud for micro wind turbines. *Renew. Energy* **2019**, *145*, 1061–1072. [[CrossRef](#)]
27. Hsiao, F.-B.; Bai, C.-J.; Chong, W.-T. The Performance Test of Three Different Horizontal Axis Wind Turbine (HAWT) Blade Shapes Using Experimental and Numerical Methods. *Energies* **2013**, *6*, 2784–2803. [[CrossRef](#)]
28. Abe, K.-I.; Ohya, Y. An investigation of flow fields around flanged diffusers using CFD. *J. Wind Eng. Ind. Aerodyn.* **2004**, *92*, 315–330. [[CrossRef](#)]
29. Pritchard, L.J. An Eleven Parameter Axial Turbine Airfoil Geometry Model. In *Volume 1: Aircraft Engine; Marine; Turbomachinery; Microturbines and Small Turbomachinery*; American Society of Mechanical Engineers: Houston, TX, USA, 1985. [[CrossRef](#)]
30. Wilcox, D.C. *Turbulence Modeling for CFD*, 3rd ed.; DCW Industries: La Cañada, CA, USA, 2006.
31. Menter, F.R. Two-equation eddy-viscosity turbulence models for engineering applications. *AIAA J.* **1994**, *32*, 1598–1605. [[CrossRef](#)]
32. Loyseau, X.; Verdin, P.; Brown, L. Scale-up and turbulence modelling in pipes. *J. Pet. Sci. Eng.* **2018**, *162*, 1–11. [[CrossRef](#)]
33. Hjort, S.; Larsen, H. A Multi-Element Diffuser Augmented Wind Turbine. *Energies* **2014**, *7*, 3256–3281. [[CrossRef](#)]
34. Shih, T.-H.; Liou, W.W.; Shabbir, A.; Yang, Z.; Zhu, J. A new k- ϵ eddy viscosity model for high reynolds number turbulent flows. *Comput. Fluids* **1995**, *24*, 227–238. [[CrossRef](#)]
35. Ostowari, C.; Naik, D. *Post-Stall Wind Tunnel Data for NACA 44XX Series Airfoil Sections*; Solar Energy Research Institute: Golden, CO, USA, 1985. [[CrossRef](#)]
36. Tavares Dias do Rio Vaz, D.A.; Mesquita, A.L.A.; Vaz, J.R.P.; Blanco, C.J.C.; Pinho, J.T. An extension of the Blade Element Momentum method applied to Diffuser Augmented Wind Turbines. *Energy Convers. Manag.* **2014**, *87*, 1116–1123. [[CrossRef](#)]
37. Hansen, M. *Aerodynamics of Wind Turbines*; Routledge: London, UK, 2015.